ACS Catalysis

Research Article

Cite This: ACS Catal. 2019, 9, 6320−6334

pubs.acs.org/acscatalysis

Effect of Zeolite Topology and Reactor Configuration on the Direct Conversion of CO_2 to Light Olefins and Aromatics

Adrian Ramirez,[†] Abhishek Dutta Chowdhury,[†] Abhay Dokania,[†] Pieter Cnudde,[‡] Mustafa Caglayan,[†] Irina Yarulina,[†] Edy Abou-Hamad,[§] Lieven Gevers,[†] Samy Ould-Chikh,[†] Kristof De Wispelaere,[‡] Veronique van Speybroeck,*[,‡] and Jorge Gascon*[,†]

[†]KAUST Catalysis Center (KCC), Advanced Catalytic Materials, King Abdullah University of Science and Technology, Thuwal 23955, Saudi Arabia

[‡]Center for Molecular Modeling, Ghent University, Technologiepark 46, B-9052 Zwijnaarde, Belgium

[§]Imaging and Characterization Core Laboratories, King Abdullah University of Science and Technology, Thuwal 23955, Saudi Arabia

Supporting Information

ABSTRACT: The direct transformation of CO_2 into high-value-added hydrocarbons (i.e., olefins and aromatics) has the potential to make a decisive impact in our society. However, despite the efforts of the scientific community, no direct synthetic route exists today to synthesize olefins and aromatics from CO_2 with high productivities and low undesired CO selectivity. Herein, we report the combination of a series of catalysts comprising potassium superoxide doped iron oxide and a highly acidic zeolite (ZSM-5 and MOR) that directly convert CO_2 to either light olefins (in MOR) or aromatics (in ZSM-5) with high space−time yields ($STY_{C2-C4=}$ = 11.4 mmol·g^{-1}·h^{-1}; STY_{AROM} = 9.2 mmol·g^{-1}·h^{-1}) at CO selectivities as low as 12.8% and a CO_2 conversion of 49.8% (reaction conditions: T = 375 °C, P = 30 bar, H_2/CO_2 = 3, and 5000 mL·g^{-1}·h^{-1}). Comprehensive solid-state nuclear magnetic resonance characterization of the zeolite component reveals that the key for the low CO selectivity is the formation of surface formate species on the zeolite framework. The remarkable difference in selectivity between the two zeolites is further rationalized by first-principles simulations, which show a difference in reactivity for crucial carbenium ion intermediates in MOR and ZSM-5.

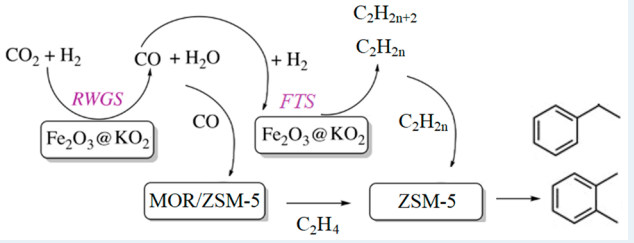

KEYWORDS: *CO_2 conversion, hydrogenation, olefins, aromatics, zeolites, bifunctional catalyst*

INTRODUCTION

Today, more than 3 gigatons of CO_2 are emitted to the atmosphere every month.[1] Undoubtedly, CO_2 levels are higher than at any point in at least the past 800 000 years, leading to a dangerous temperature increase at the Earth's surface.[2] In this scenario, methods to transform this greenhouse gas into valuable chemicals may help address (at least partially) this pressing challenge.[3] Indeed, the development of technologies that turn CO_2 into valuable chemicals is gaining momentum in the scientific and industrial communities.[4,5]

One of the most promising approaches toward CO_2 reductive valorization consists of the combination of conventional metallic catalysts with acidic zeolites.[6] This combination has been shown to enable the direct transformation of CO_2 to chemicals with selectivities for either light olefins (C_2−C_4) or aromatics above the limitation of classical Fischer−Tropsch synthesis (FTS), as defined by the Anderson−Schulz−Flory (ASF) distribution.[7,8] In these bifunctional systems, the conversion of CO_2 to hydrocarbons can proceed through two different routes: (i) the transformation of CO_2 into CO via reverse water−gas shift (RWGS) and subsequent conversion of CO to hydrocarbons via the classical Fischer−Tropsch mechanism,[9] followed by hydrocarbon cracking, isomerization, aromatization, etc. on the zeolite;[10] (ii) the transformation of CO_2 into methanol,[11] followed by its conversion into hydrocarbons over the zeolite framework via the classical methanol-to-hydrocarbons (MTH) mechanism.[12,13]

However, due to the lack of efficient catalysts for the first step (activation of CO_2), productivities reported to date are low (see Table S1 for a complete overview of the state-of-the-art for CO_2 conversion via bifunctional catalyst). In addition, multiple reactions are involved (oligomerization, cracking, dehydrogenation, cyclization, alkylation, isomerization, etc.), and many intermediates can serve as reactants in competitive reaction pathways, impeding the complete understanding of the global reaction mechanism.[14,15] Moreover, in most of the bifunctional systems reported, the selectivity to undesired CO represents more than half of the total products.[16−20] As direct consequence, many studies unfairly exclude the high CO

Received: April 10, 2019
Revised: May 26, 2019
Published: May 29, 2019

DOI: 10.1021/acscatal.9b01466
ACS Catal. 2019, 9, 6320−6334

selectivity when showing reaction data, thus reporting unrealistic catalyst CO free selectivities.

To overcome the limitations of the above materials, we have developed a novel catalyst combination comprising potassium superoxide-doped iron oxide and a highly acidic zeolite. The potassium superoxide-doped iron oxide stand-alone catalyst (Fe_2O_3@KO_2) was recently reported by our group[21] and yields productivities in the order of commercial FTS materials. Here we go one step forward and combine this material with highly acidic zeolites to fine-tune the product distribution to either light olefins (C_2−C_4=) or aromatics. In particular, we have chosen ZSM-5 owing to the well-known ability of the MFI topology to generate aromatics[22] and mordenite (MOR) due to its ethylene shape selectivity within the 8-membered ring (8MR).[23,24] When the two components are placed together in a single reactor, high selectivities for either light olefins (via MOR) or aromatics (via ZSM-5) and high values of space−time yields with minimal selectivities for undesired CO and CH_4 are achieved. In-depth characterization via magic angle spinning (MAS) solid-state nuclear magnetic resonance (ssNMR) spectroscopy on both spent zeolites reveals that the reaction mechanism is primarily driven by the incorporation of CO in the network in the form of surface formate species. Ab initio simulations further demonstrate a difference in stability of long-chain alkene intermediates on ZSM-5 and MOR. As carbenium ions are crucial intermediates for the conversion of hydrocarbons in zeolites, the different product distribution in the two zeolites can be attributed to the ability of these two zeolites to activate alkenes toward aromatics formation or cracking reactions.

MATERIALS AND METHODS

Chemicals. Iron oxide (Fe_2O_3, Aldrich), potassium superoxide (KO_2, Aldrich), sodium aluminate ($NaAlO_2$, Aldrich), tetrapropylammonium hydroxide (TPAOH, Aldrich), tetraethyl orthosilicate (TEOS, Aldrich), ammonium nitrate (NH_4NO_3, Aldrich), and ZSM-5 (SiO_2/Al_2O_3 = 26, SiO_2/Al_2O_3 = 52, SiO_2/Al_2O_3 = 300, ACS Materials) were used as received. Mordenite (SiO_2/Al_2O_3 = 20, Alfa Aesar) was calcined at 550 °C for 7 h prior to its use. ZSM-5 with SiO_2/Al_2O_3 = 26 was always used unless otherwise stated.

Catalyst Preparation. The Fe_2O_3@KO_2 catalyst was obtained by mortar mixing of Fe_2O_3 and KO_2, keeping a molar ratio of Fe/K = 2. The resultant mixture was heated to 100 °C for 12 h prior to the catalytic measurements. ZSM-5 with SiO_2/Al_2O_3 = 600 was synthesized in our laboratory by the following procedure: $NaAlO_2$ (0.010 g), TPAOH (16.8 mL, 1 M in H_2O), and TEOS (8.4 mL) were mixed in water (15.6 mL) and aged at 100 °C for 2 h. After being stirred overnight at room temperature, the mixture was transferred into an autoclave at 180 °C for 20 h for further crystallization. The collected solid was centrifuged and washed until pH 7 was reached. Following, the sample was calcined at 550 °C for 7 h. Due to the presence of Na ions on the zeolite, an ion-exchange step was applied with 1 M NH_4NO_3 solution. Afterward, the zeolite was again calcined at 550 °C for 7 h.

CO_2 Hydrogenation Tests. Catalytic tests were executed in a 16-channel Flowrence platform from Avantium. Typically 50 mg of the stand-alone Fe_2O_3@KO_2 catalyst and 100 mg of composite catalyst with Fe_2O_3@KO_2/zeolite with mass ratio 1/1 in a dual-bed configuration were used. The mixed feed had 25 vol% of CO_2 and 75 vol% of H_2. In addition, 8 mL/min of He was mixed with the feed as internal standard. We aimed to have 10 000 mL·g^{-1}·h^{-1} per channel in the stand-alone catalyst and 5000 mL·g^{-1}·h^{-1} in the composite catalyst. The 16th channel was always left without catalyst as blank. The reaction temperature was typically set at 375 °C. Prior to feeding the reaction mixture, all samples were pre-treated in situ with a pure H_2 atmosphere for 4 h at 350 °C. The tubes were then pressurized to 30 bar using a membrane-based pressure controller.

An Agilent 7890B gas chromatograph with two sample loops was used. After the loops were flushed for 24 min, the content was injected. One sample loop goes to a TCD channel with 2 Haysep pre-column and MS5A, where He, H_2, CH_4, and CO are separated. Gases that have longer retention times than CO_2 on the Haysep column (Column 4 Haysep Q, 0.5 m, G3591-80023) are back-flushed. Further separation of permanent gases is done on another Haysep column (Column 5 Haysep Q, 6 ft, G3591-80013) to remove CO_2 before going to MS5A. CO_2 is sent to a channel with a restrictor to avoid CO_2 on MS5A. Another sample loop goes to an Innowax pre-column (5 m, 0.20 mm o.d., 0.4 μm film). For the first 0.5 min of the method, the gases coming from the pre-column are sent to a Gaspro column (Gaspro 30 m, 0.32 mm o.d.) followed by a flame ionization detector (FID). After 0.5 min, the valve is switched, and the gases are sent to an Innowax column (45 m, 0.2 mm o.d., 0.4 μm) followed by a FID. The Gaspro column separates C_1−C_8, paraffins, and olefins. Innowax separates larger parafins and olefins (>C_9), benzene/toluene/xylene (BTX), and C_9+ aromatics.

Conversion (X, %), space−time yields (STY, mmol·g·cat^{-1}·h^{-1}), and selectivities (S, %) are defined as follows:

$$X_{CO_2} = \left(1 - \frac{C_{He,blk} C_{CO_2,R}}{C_{He,R} C_{CO_2,blk}}\right) \times 100$$

$$S_{Cn} = \frac{n\left(\frac{C_{Cn,R}}{C_{He,R}}\right)}{\left(\frac{C_{CO_2,blk}}{C_{He,blk}} - \frac{C_{CO_2,R}}{C_{He,R}}\right)} \times 100$$

$$STY_{C2\text{-}C4=} = \frac{X_{CO_2}/100 \times S_{C2\text{-}C4=}/100 \times GHSV_{CO_2}}{22.4}$$

where $C_{He,blk}$, $C_{He,R}$, $C_{CO_2,blk}$, and $C_{CO_2,R}$ are the concentrations determined by GC analysis of He in the blank (blk), He in the reactor (R) effluent, CO_2 in the blank, and CO_2 in the reactor effluent, respectively, $C_{Cn,R}$ is the concentration of the reactor effluent determined by GC analysis of a product with n carbon atoms, and $GHSV_{CO_2}$ is the CO_2 gas space−time velocity in mL·g·cat^{-1}·h^{-1}. The error in carbon balance was better than 2.5% in all cases.

Nitrogen Adsorption Measurements. Nitrogen adsorption and desorption isotherms were recorded on a Micromeritics ASAP 2040 system at 77 K. Samples were previously evacuated at 373 K for 16 h. The Brunauer−Emmett−Teller (BET) method was used to calculate the surface area. The p/p_0 range for BET analysis was $0.067 < p/p_0 < 0.249$.

X-ray Diffraction (XRD) Measurements. XRD patterns were obtained using Bruker D8 equipment in Bragg−Brentano configuration using Cu Kα radiation. The diffractograms were scanned with a step size of 0.02° in the 2θ range of 20−80°. The crystalline phase was identified by comparison with data from the Inorganic Crystal Structure Database (ICSD).

DOI: 10.1021/acscatal.9b01466
ACS Catal. 2019, 9, 6320−6334

Temperature-Programed Desorption (TPD) Measurements. TPD experiments were carried out on a Micromeritics ASAP 2020 analyzer. The catalyst samples were first heated in a helium flow at 350 °C for 4 h, followed by cooling to 50 °C. After cooling, the zeolites were saturated in ammonia, and the temperature of the samples was increased linearly at a rate of 10 K·min^{-1}. Ammonia was fed at atmospheric pressure with a 5 vol% NH_3 concentration diluted in helium. The ammonia desorption was continuously monitored by a thermal conductivity detector.

Inductively Coupled Plasma (ICP) Measurements. The analyses were carried out on an ICP−optical emission spectrometer after digestion of the solid samples. Complete digestion of the powder samples was achieved using aqua regia in a ratio of 1 mg of catalyst:1 mL of aqua regia for 24 h at room temperature.

Electron Microscopy and Elemental Mapping. Transmission electron microscopy (TEM) of the samples was performed with a Titan Themis-Z microscope from Thermo Fisher Scientific by operating it at an accelerating voltage of 300 kV and with a beam current of 0.5 nA. Dark-field imaging was performed by scanning TEM (STEM) coupled to a high-angle annular dark-field (HAADF) detector. The STEM-HAADF data were acquired with a convergence angle of 29.9 mrad and a HAADF inner angle of 30 mrad. Furthermore, an X-ray energy dispersive spectrometer (FEI SuperX, ∼0.7 srad collection angle) was also utilized in conjunction with DF-STEM imaging to acquire STEM-energy dispersive spectrometry (EDS) imaging data sets (image size 1024 × 1024 pixels, dwell time 5 μs). During the acquisition of these data sets, at every image pixel, a corresponding EDS spectrum was also acquired to generate simultaneously the elemental maps of Fe, O, C, and K atoms. It is also pertinent to note herein that spectrum-imaging data sets were acquired in so-called frame mode, in which the electron beam was allowed to dwell at each pixel for only a few microseconds in order to keep the total frame time to 6 s or less. Both imaging and spectroscopy data sets for each sample were acquired as well as analyzed with a newly developed software package called Velox from Thermo Fisher Scientific. The elemental maps for Fe, O, C, and K atoms were computed using the extracted intensities of their respective Kα lines after background subtraction. The generated maps were slightly post-filtered by applying a Gaussian filter (σ = 0.5).

Nuclear Magnetic Resonance Measurements. The MAS ssNMR spectroscopic experiments were performed on Bruker AVANCE III spectrometers operating at 400 MHz frequency for ^{1}H using a conventional double-resonance 4 mm CPMAS probe (CP = cross-polarization). NMR chemical shifts are reported with respect to the external reference adamantane. For ^{1}H−^{13}C CP experiments, the following sequence was used: 90° pulse on the proton (pulse length 2.4 s), then a CP step with the contact time of typically 2 ms, and finally acquisition of the ^{13}C NMR signal under high-power proton decoupling. The delay between the scans was set to 5 s to allow complete relaxation of the ^{1}H nuclei, and the number of scans is mentioned in the respective figure captions. An exponential apodization function corresponding to a line broadening of 80 Hz was applied prior to Fourier transformation. The 2D ^{1}H−^{13}C heteronuclear correlation (HETCOR) ssNMR spectroscopy experiments were performed according to the following scheme: 90° proton pulse, t_1 evolution period, CP to ^{13}C, and detection of the ^{13}C magnetization under two-pulse phase modulation (TPPM) decoupling. For the CP step, a ramped radio frequency (RF) field centered at 75 kHz was applied to the protons, while the ^{13}C channel RF field was matched to obtain an optimal signal. Using a short contact time (0.2 ms) for the CP step, the polarization transfer in the dipolar correlation experiment was verified to be selective for the first coordination sphere to lead to correlations only between pairs of attached ^{1}H−^{13}C spins (C−H directly bonded). 2D ^{13}C−^{13}C spectra were recorded using a 2 s recycle delay as well as 10 ms (F2) and 6 ms (F1) acquisition times. Herein, carbons were polarized via CP, and ^{13}C−^{13}C mixing was achieved through proton-driven spin diffusion using phase-alternated recoupling irradiation schemes (PARIS) for 30 ms. ^{39}K MAS ssNMR was performed on 900 MHz Bruker AVANCE IV 21.1 T spectrometers quipped with 4 mm CPMAS probes. ^{39}K shifts were referenced to KBr, and typically a recycle delay of 1 s was used.

Computational Methodology. To rationalize the difference in selectivity between the two catalysts, a series of first-principles static and molecular dynamics (MD) simulations were performed in H-ZSM-5 and H-MOR according to general principles outlined in the work of V. Van Speybroeck et al.[25] All calculations were performed on fully periodic models of H-ZSM-5 and H-MOR. For H-ZSM-5, a single unit cell containing 96 T atoms has been used, while for H-MOR, a 1×1×2 super cell consisting of 96 T atoms has been used. Each catalyst model contains a single Brønsted acid site (BAS) per unit cell, which is created by substituting a Si atom by an Al atom and adding a charge-compensating proton. Both zeolites exhibit a fundamentally different channel system. H-ZSM-5 has the MFI topology, characterized by perpendicularly intersecting straight (5.3 Å × 5.6 Å) and sinusoidal (5.1 Å × 5.5 Å) 10-ring channels.[26] Al substitution was done at the T12 site, i.e., at the intersection of the straight and sinusoidal channels (Figure S1A). This location offers maximal accessibility for reacting guest molecules and is therefore the most common acid site position in modeling studies.[27] H-mordenite has the MOR topology, characterized by parallel 8-ring (2.6 Å × 5.7 Å) and 12-ring (6.5 Å × 7.0 Å) straight channels which are connected via 8-ring side pockets.[26] In H-MOR, the active site can be located at four different framework positions (Figure S1B) which result in different local environments for the adsorbates. The T1 site is situated at the intersection of the 12-ring channel and the 8-ring channel. This location provides a maximal amount of space for the adsorbed molecules, which can reside in the main 12-ring channel. The T2/T4 sites are located at the intersection of the 12-ring channel and the 8-ring side pocket, which provides partial confinement as adsorbates need to (partly) diffuse into the side pocket to approach this active site. The T3 site is found at the intersection of the 8-ring channel and the 8-ring side pocket. Bulky, long-chained molecules, however, are sterically hindered to diffuse into the 8-ring channel. Therefore, this active site will only be accessible for small molecules. In this study, the Al substitution is placed either at the T1 or T2 site, which will be further denoted as zeolite MOR-1 and MOR-2, respectively.

Periodic density functional theory (DFT) calculations were performed with the Vienna Ab Initio Simulation Package (VASP 5.4.1).[28−31] Optimized geometries were obtained using the conjugate gradient method. For all calculations, the PBE functional[32] with additional Grimme D3 dispersion corrections[33] was used. The projector augmented wave (PAW) approximation[34,35] was applied, and sampling of the Brillouin

DOI: 10.1021/acscatal.9b01466
ACS Catal. 2019, 9, 6320−6334

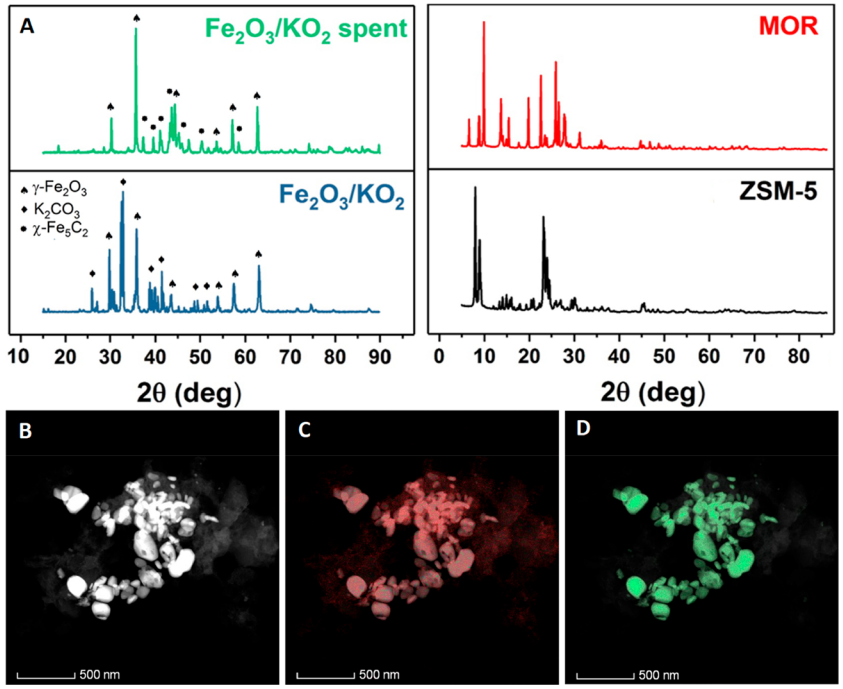

Figure 1. Characterization of the bifunctional Fe_2O_3@KO_2/zeolite material. (A) XRD patterns of the commercial zeolites and the fresh and spent stand-alone Fe catalyst. (B) TEM image of the stand-alone Fe catalyst activated under reaction conditions. K (C) and Fe (D) elemental mapping of the stand-alone Fe catalyst activated under reaction conditions.

zone was restricted to the Γ-point. The plane wave energy cutoff was set to 600 eV. The threshold for the electronic self-consistent field (SCF) calculations was fixed at 10^{-5} eV. The nature of the stationary points was verified by a normal-mode analysis using partial Hessian vibrational analysis (PHVA)[36−38] on the adsorbates and an 8T cluster of the framework, centered around the acid site. To determine the adsorption enthalpy and free energy, thermal corrections were estimated based on the harmonic oscillator (HO) approximation with the in-house-developed processing toolkit TAMkin.[39]

Ab initio MD simulations were carried out with the CP2K software package (CP2K 3.0).[40] The revPBE functional[41] with inclusion of Grimme D3 dispersion corrections[33] was chosen as the level of theory. The DZVP-GTH basis set,[42] which is a combination of Gaussian basis functions and plane waves[43,44] with a cutoff energy of 320 Ry, was used for all atoms. The SCF convergence criterion was fixed at 10^{-6} eV. All simulations were performed in the NVT ensemble using a time step of 0.5 fs. The temperature (350 °C) was controlled by a chain of five Nosé−Hoover thermostats.[45,46] Unit cell parameters were determined from a preliminary 10 ps MD run in the NpT ensemble at 350 °C and 1 bar, which was controlled by an MTK barostat (see Table S2).[47] All systems were first equilibrated for 5 ps, followed by a production run of 100 ps to obtain a sufficient sampling of the phase space. The plane wave kinetic energy cutoff was set to 600 eV. The threshold for the electronic self-consistent cycle was set at 10^{-5} eV, while the ionic convergence criterion was set at 10^{-4} eV for all relaxations.

Umbrella sampling (US) simulations were performed with CP2K as MD engine, interfaced with the advanced simulation library PLUMED.[48] To sample the activated transition from an alkene to a carbenium ion, a predefined reaction coordinate or collective variable (CV) was used. The protonation of a linear alkene can be described by a single CV based on a coordination number (CN), which is defined as

$$\mathrm{CN} = \sum_{i,j} \frac{1 - (r_{ij}/r_0)^{\mathrm{nn}}}{1 - (r_{ij}/r_0)^{\mathrm{nd}}}$$

in which the sum runs over two sets of atoms i and j with r_{ij} the interatomic distance between atom i and atom j, and r_0 a reference distance. The parameters nn and nd are set at 6 and 12, respectively. To describe the proton transfer from the zeolite (z) to the hydrocarbon (hc), a CN between the oxygen atoms of the acid site (O_z) and the hydrogen atoms of the hydrocarbon (H_{hc}) (see Figure S2) is used as CV.[49] A reference distance of 1.25 Å was selected.

The CV was divided into 32 equidistant windows. For each window, a regular 25 ps MD simulation with an additional harmonic bias potential was carried out to ensure each part of the reaction is equally well sampled.[50] The bias potential has a spring constant of 3000 kJ·mol^{-1}. The MD simulations were initiated from configurations that were randomly obtained from a moving bias potential simulation, describing the entire range of the reaction coordinate. For the US simulations, the TZVP-GTH basis was used, which allows for an improved description of the host−guest interactions. All other MD settings remained unchanged. Ultimately, the free energy profile was reconstructed from the sampling distribution in each window, using the weighted histogram analysis method (WHAM).[51,52]

RESULTS

Catalytic Performance of the Bifunctional Systems on the CO_2 Hydrogenation Reaction. Synthesis of the stand-alone Fe-based catalyst was done according to our recent work.[21] Briefly, we prepared Fe_2O_3@KO_2 catalyst by mortar mixing commercial iron oxide and commercial potassium

DOI: 10.1021/acscatal.9b01466
ACS Catal. 2019, 9, 6320−6334

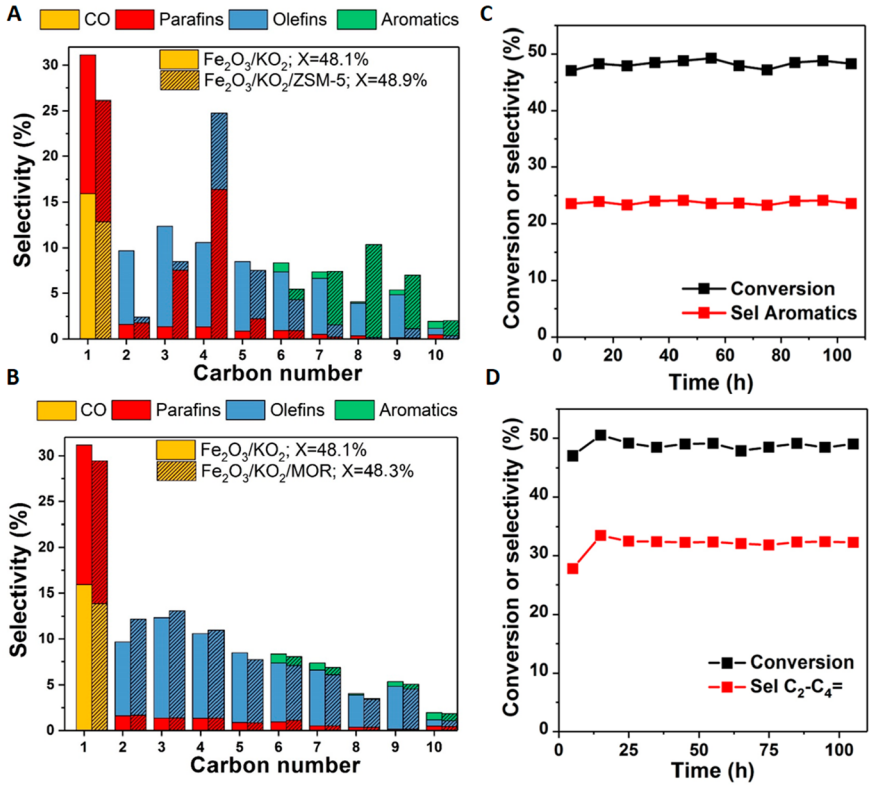

Figure 2. Catalytic performance of the bifunctional Fe_2O_3@KO_2/zeolite system. (A) Product distribution of the Fe_2O_3@KO_2/ZSM-5 and Fe_2O_3@KO_2 catalysts after 50 h TOS. (B) Product distribution of the Fe_2O_3@KO_2/MOR and Fe_2O_3@KO_2 catalysts after 50 h TOS. (C) Stability of the Fe_2O_3@KO_2/ZSM-5 bifunctional catalyst during 150 h TOS. (D) Stability of the Fe_2O_3@KO_2/MOR bifunctional catalyst during 150 h TOS. Reaction conditions: 375 °C, 30 bar, H_2/CO_2 = 3, and 5000 mL·g^{-1}·h^{-1}.

superoxide, keeping a molar Fe/K ratio of 2. Figure 1A shows the XRD patterns of the commercial zeolites (MOR and ZSM-5) and the fresh and used stand-alone Fe_2O_3@KO_2 after 50 h time-on-stream (TOS) at 375 °C, 30 bar, H_2/CO_2 = 3, and 10000 mL·g^{-1}·h^{-1}. In the fresh catalyst, a mixture of magnetite and potassium carbonate can be observed, while on the spent catalyst, no trace of the crystalline potassium carbonate is observed and the iron oxide is partially transformed to iron carbide, Fe_5C_2. STEM was used to further investigate the properties of the Fe_2O_3@KO_2 catalyst after reaction. In accordance with our previous work, the Fe_2O_3@KO_2 catalyst is composed mainly of a carbonaceous structure containing large amounts of cationic K (see Figure S3), homogeneously distributed over the matrix along with nanosized Fe (see Figure 1D). Both commercial zeolites were also characterized by means of ICP, BET, and ammonia TPD, showing values close to the ones provided by the manufacturer (see Figure S4 and Table S3).

The detailed performance of the stand-alone Fe_2O_3@KO_2 catalyst in the hydrogenation of CO_2 after 50 h TOS at 375 °C, 30 bar, and H_2/CO_2 = 3 is summarized in Table S4. The CO_2 conversion for this catalyst is 48.1%, with a total olefin selectivity of 57.4%, a CH_4 selectivity of 15.2%, and a CO selectivity of only 15.9%. This catalytic performance is stable during at least 100 h TOS (see Figure S5). The light olefins fraction accounts for 49.3% of the total olefins, with a total olefin/paraffin ratio of 8.5. This product distribution is shifted drastically by assembling the bifunctional system incorporating a zeolite (MOR or ZSM-5) in a dual bed configuration with a 1/1 mass ratio. The addition of highly acidic ZSM-5 enhances the formation of aromatics (see Figure 2A). The selectivity of aromatics increases to 61.4% in the liquid fraction (C_{5+}). However, this aromatic increase is accompanied by a decrease of the C_2−C_{10} olefins and the formation of isobutane as main byproduct. The aromatic distribution is presented in Figure S6. We detected aromatics up to C_{10}, toluene being the most abundant aromatic compound formed, followed by xylenes and C_9 aromatics.

In a similar but different manner, the addition of MOR shifts the product distribution by enhancing the formation of ethylene and propylene, the two most highly demanded olefins (see Figure 2B). In particular, total selectivities to ethylene and propylene of 11.5% and 12.5% can be achieved. Interestingly, MOR does not seem to be active in hydrocarbon cracking, since the yields of most hydrocarbon fractions (except for the above-mentioned C_2 and C_3 fractions) remain almost unchanged. Both bifunctional systems are stable under reaction conditions for at least 100 h (see Figure 2C,D). On an additional note, the CO_2 conversion remains invariable for both MOR and ZSM-5 systems in comparison with the bare Fe_2O_3@KO_2 catalyst and with good reproducibility between different batches (see Table S5).

In line with some previous reports,[53] CO selectivity decreases upon incorporation of a zeolite component. In particular, in the Fe_2O_3@KO_2/MOR the CO selectivity is 13.7% while in the Fe_2O_3@KO_2/ZSM-5 it is as low as 12.8%, the lowest values reported for this kind of systems (see Table S1). This effect was further evaluated by performing CO co-feeding experiments. The addition of CO to the feed significantly increases the conversion for both bifunctional systems (see Table 1), which indirectly indicates the existence of carbonylated reactive intermediates during the reaction.

DOI: 10.1021/acscatal.9b01466
ACS Catal. 2019, 9, 6320−6334

Table 1. Effect of CO Co-feeding on the Fe_2O_3@KO_2/Zeolite Bifunctional Catalysts[a]

catalyst	CO co-feed	conv[b] (%)	selectivity (%)		
			C_1	arom	C_2-C_4=
Fe_2O_3@KO_2/ZSM-5	no	48.9	13.9	24.9	12.1
Fe_2O_3@KO_2/ ZSM-5	yes	58.4	19.5	28.4	11.1
Fe_2O_3@KO_2/MOR	no	48.3	14.5	2.6	33.3
Fe_2O_3@KO_2/MOR	yes	57.9	20.7	3.0	38.3

[a]Reaction conditions: 30 bar, $H_2/(CO+CO_2)$ = 3, CO/CO_2 = 1, and 5000 mL·g^{-1}·h^{-1}. [b]Total carbon (CO + CO_2) conversion.

Furthermore, the addition of CO to the feed also increases selectivity to olefins and aromatics, achieving a total C_2−C_4 olefin selectivity of 38.3% with a carbon conversion of 57.9% in the Fe_2O_3@KO_2/MOR catalyst and a total aromatic selectivity of 28.4% with a carbon conversion of 58.3% in the Fe_2O_3@KO_2/ZSM-5 catalyst at 375 °C (see Table 1).

The effect of the catalyst spatial arrangement was studied for both bifunctional systems (see Figure S7). When the spatial arrangement was changed from dual bed to a mortar-mixed system, the performance was inferior in both systems, yielding carbon monoxide as the primary product. These results suggest that the acidity of the zeolite is poisoning the K basicity of the catalyst and vice versa, in accordance with previous reports.[8] It also suggests the high mobility of K in our catalytic system, which could indeed be rationalized by ssNMR spectroscopy.[21] In addition, for the particular system of ZSM-5, the effect of the SiO_2/Al_2O_3 ratio was also evaluated. Figure 3A shows that, upon increasing the SiO_2/Al_2O_3 ratio, the total aromatic selectivity decreases. Interestingly, a linear relationship was observed between the aromatics produced and the paraffins formed as byproducts, with isobutane as the main co-product in all cases (see Figure 3B). This trend is line with previous works, with isobutane being the main byproduct of the ethylene/propylene/butene aromatization, closely followed by propane.[14] H-transfer reactions, which play a key role in the formation of both aromatics and paraffins from light olefins, are the main driving force behind this effect.[54]

The effect of the reaction conditions was further evaluated by performing CO_2 hydrogenation tests at different reaction temperatures (325, 350, and 375 °C) and pressures (20, 30, and 40 bar). For the Fe_2O_3@KO_2/ZSM-5 combination, it can be observed that reaction temperatures of 325 °C are not enough to completely trigger the aromatization mechanism in ZSM-5. On the other hand, similar aromatics selectivities are obtained at 350 and 375 °C (see Figure S8). Varying the pressure had less effect on the aromatics selectivity while, not surprisingly, increasing the pressure led to higher CO_2 conversions (up to 53.8%) and vice versa. For the Fe_2O_3@KO_2/MOR system (see Figure S9), an increase of the olefin selectivity with the pressure is observed, regardless of the reaction temperature, achieving a total C_2−C_4 light olefins selectivity of 35.2% with a CO_2 conversion of 54.1% at 375 °C and 40 bar. In addition, unlike the case with ZSM-5, 325 °C seems to be sufficient to trigger the light olefin formation mechanism in this MOR system.

Solid-State NMR Characterization of the Spent Zeolites. To obtain some insight into the reaction mechanisms and derive structural information on zeolite-trapped species, advanced MAS ssNMR was performed on the post-reacted zeolite materials. In the 1D ^1H−^{13}C CP spectra (Figure S10), two predominant features were observed: (i) 8−40 ppm aliphatic and methyl groups and (ii) 120−158 ppm olefinic and/or aromatic moieties. On a closer look, the lack of signal for the unsaturated species specifically on the post-reacted MOR sample indicates the plausible non-existence of aromatic species. Alternatively, a relatively more intense signal on the post-reacted zeolite ZSM-5 (even with the lower number of scans) over zeolite MOR suggests relatively more efficient CP transfer in the former case, implying it is a relatively more hydrogen-rich system (Figure S10). Thermogravimetric analysis further confirms the existence of a hydrogen-deficient system in the MOR (Figure S11), as low hydrogen-to-carbon ratio coke (i.e., removed at temperatures above 550 °C) accounts for a total 12.7% weight loss in the spent MOR compared with the 4.5% observed in the spent ZSM-5. Next, 2D ^1H−^{13}C CP-HETCOR experiments were performed for ^1H−^{13}C correlations on both post-reacted zeolites (Figures 4 and 5), which clearly distinguishes their non-identical nature.

In MOR, olefinic carbons were typically correlated to both olefinic and aliphatic methyl hydrogens, which indicates that

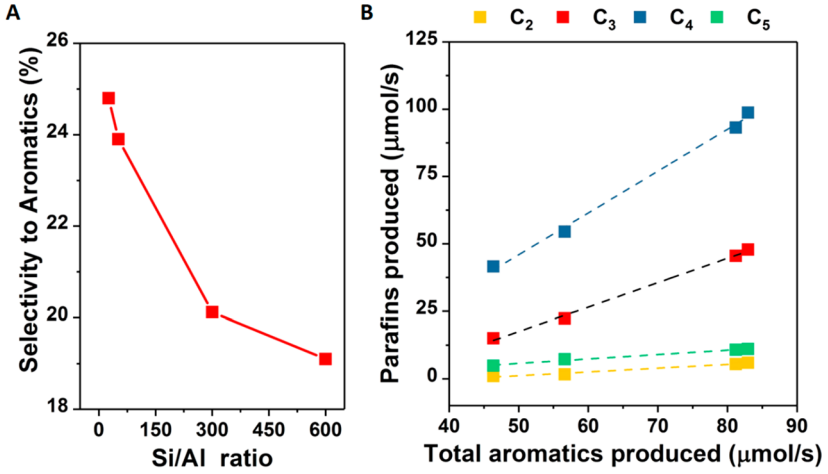

Figure 3. Effect of zeolite properties on the catalytic performance of the Fe_2O_3@KO_2/ZSM-5 bifunctional system. (A) Effect of the SiO_2/Al_2O_3 ratio on the aromatic selectivity. (B) Molar relationship between aromatics and the paraffins produced for the different SiO_2/Al_2O_3 ratios tested. Reaction conditions: 375 °C, 30 bar, H_2/CO_2 = 3, 5000 mL·g^{-1}·h^{-1}, and 50 h TOS.

DOI: 10.1021/acscatal.9b01466
ACS Catal. 2019, 9, 6320−6334

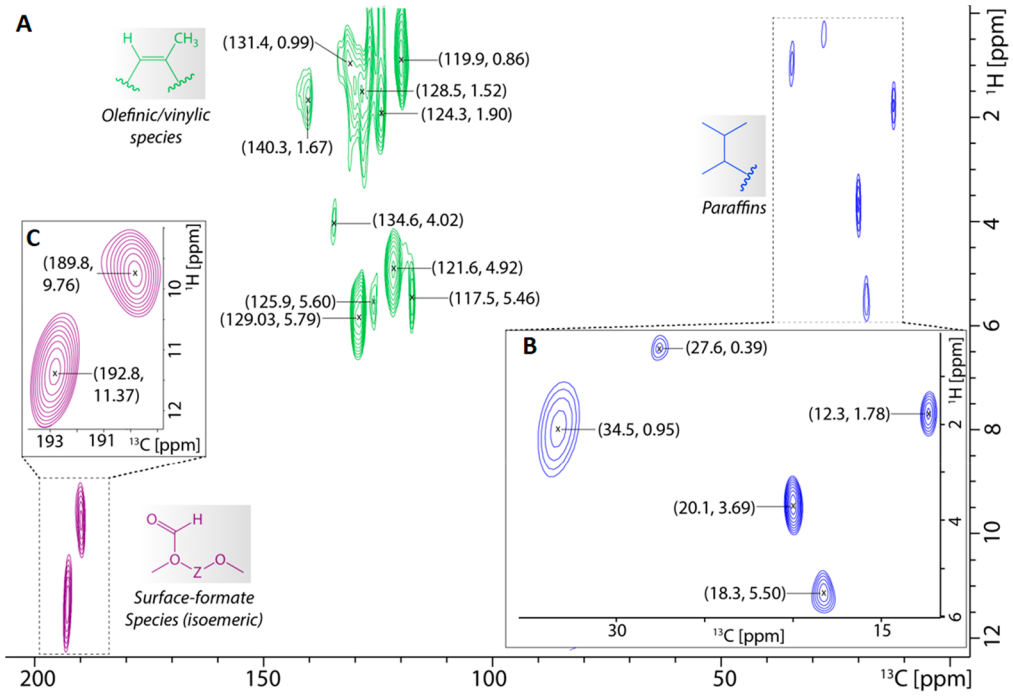

Figure 4. 2D MAS $^{1}H-^{13}C$ cross-polarization HETCOR ssNMR correlations of identified zeolite MOR trapped molecular scaffolds: olefinic/vinylic (in light green), aliphatic (in blue), and carbonyl (in purple). (A) Spectra obtained on the post-reacted MOR after the hydrogenation of carbon dioxide over Fe_2O_3@KO_2/MOR for 50 h. Herein, dipolar cross-polarization was used to polarize carbons in this correlation spectrum. Zooms of (B) aliphatic and (C) carbonyl regions are displayed separately (number of scans = 3504).

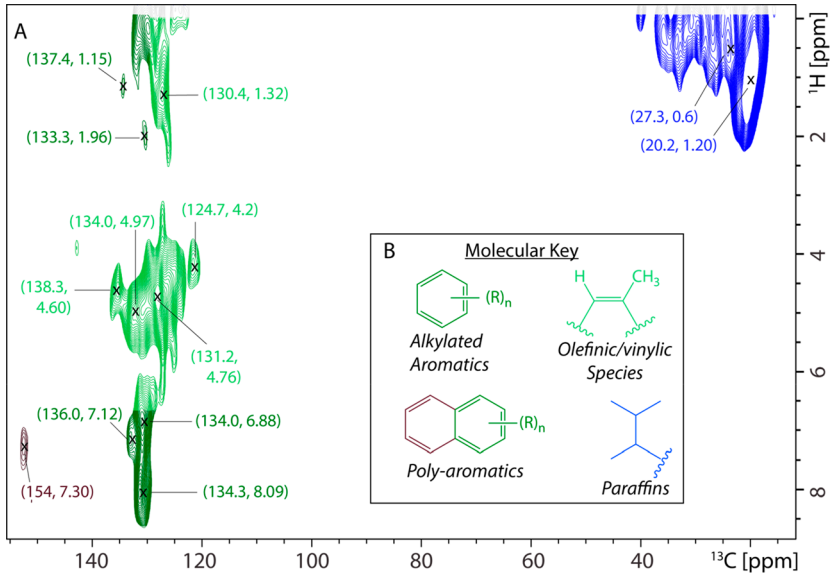

Figure 5. 2D MAS $^{1}H-^{13}C$ cross-polarization HETCOR ssNMR correlations. (A) Spectra obtained on the post-reacted ZSM-5 after the hydrogenation of carbon dioxide over Fe_2O_3@KO_2/ZSM-5 for 50 h. (B) Identified zeolite ZSM-5-trapped molecular scaffolds: olefinic/vinylic (in light green), mono-aromatics (in green), poly-aromatics (in brown), and aliphatic (in blue) (number of scans = 2496).

alkylated olefinic/vinylic species were the primary trapped organics (Figure 4). In the carbonyl region, two carbon signals at 189.8 and 192.8 ppm (typically a ketonic carbonyl region) correlate with a H-signal around 9.5−12 ppm, which could be attributed to surface formate species (Figure 4). These two signals presumably could appear due to the existence of surface formate species in a non-identical environment, such as in 8- and 12-membered rings within MOR.

Similarly, in the 2D $^{1}H-^{13}C$ CP-HETCOR spectra on ZSM-5, alkylated aromatics/poly-aromatics and olefinic/vinylic species, as well as paraffins, were distinguishable (Figure 5). Herein, we also identified that signals were relatively sharper/narrower in MOR than ZSM-5, which either could be due to the mobility of zeolite-trapped species or because they may reside in one exclusive conformation/environment in the zeolite framework.[55−58]

Although the NMR samples were prepared using naturally abundant reactants, we still have attempted to perform 2D $^{13}C-^{13}C$ correlation spectroscopy, only on the post-reacted ZSM-5 material (i.e., a more hydrogen efficient system than

DOI: 10.1021/acscatal.9b01466
ACS Catal. 2019, 9, 6320−6334

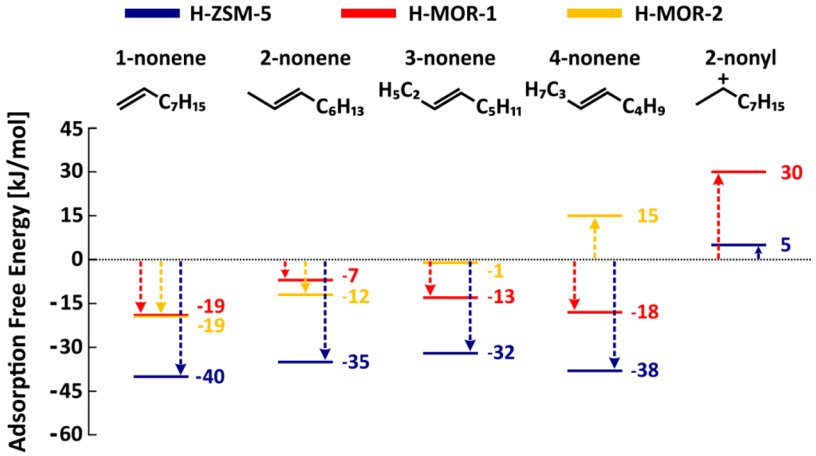

Figure 6. Adsorption free energy at 350 °C for 1-, 2-, 3-, and 4-nonene and 2-nonyl carbenium ion in H-ZSM-5, H-MOR-1, and H-MOR-2 with the empty framework and the respective *n*-nonene in the gas phase as reference state. For the carbenium ion, gas-phase 1-nonene and the empty framework are chosen as reference (level of theory: PBE-D3).

MOR), with an aim to investigate the heterogeneity of the sample as well as the zeolite-trapped C1 species (Figure S12A,B). In general, this measurement also reveals the existence of the alkylated aromatic/polyaromatic/olefinic species (Figure S12A), which is consistent with our other observations. Moreover, 2D $^{13}C-^{13}C$ spectra between 48 and 68 ppm illuminated the presence of several (albeit lower quantity) zeolite-surface bound oxygenated species (Figure S12B). In this region, two binding modes each of methanol and dimethyl ether on zeolite were identified.[56,57] The assignment of surface-adsorbed methanol species was further confirmed by a separate chemisorption experiment (Figure S12C). The line width of the 57 ppm peak (belonging to surface methoxy species, SMS) is only significantly broader, suggesting heterogeneity in its molecular environment.[58] Interestingly, another strong cross-peak between 57.1 and 47.1 ppm indicates the close proximity of SMS and surface-adsorbed methanol.[57] In principle, such close proximity is indicative of their reaction through the polarization of the C−H bond of SMS by a neighboring adjacent oxygen to form direct carbon−carbon bonds, possibly through the carbene-like reaction intermediate.[57] Additionally, as also indicated above, we have detected the migration of potassium as a hydrated potassium species (i.e., $K(H_2O)_8^+$) formed in situ by high-field ^{39}K ssNMR spectroscopy from the metallic to the zeolitic component during the reaction (see Figure S13).[59]

Theoretical Calculations on the Role of the Zeolite Framework. To obtain nanoscopic insight into the adsorption, mobility, and reactivity of alkene intermediates in ZSM-5 and MOR, a comprehensive set of theoretical calculations has been undertaken on C_9 alkenes. We investigated 1-nonene as a model component because the C_9 fraction appears to be unreactive on MOR, while it is almost entirely converted into aromatics on ZSM-5 (see Figure 2). Furthermore, a great fraction of the aromatics produced contain nine carbons (see Figure S6) and were also detected trapped in the ZSM-5 framework (see Figure S12A). This C_9 aromatics fraction is likely formed via direct cyclization of adsorbed nonene that typically takes place through carbenium ion intermediates.[27,60−65] Additionally, as double bond isomerizations are known to readily occur,[66−68] the other *n*-nonene compounds are also included in this study.

Upon adsorption of an alkene in a Brønsted acid zeolite, four different adsorption states can be formed, as shown in Figure S14: (i) a physisorbed van der Waals (vdW) complex, characterized only by dispersion interactions with the zeolite wall; (ii) a physisorbed π-complex, in which the double C=C bond forms a π-H interaction with the Brønsted acid site; (iii) a chemisorbed carbenium ion, formed via protonation of the alkene; and (iv) a chemisorbed alkoxide, which is covalently bonded to the framework. Previously, we showed that alkoxides are unstable for C_4-C_8 alkenes at elevated temperature,[69,70] an observation which can likely be extrapolated to C_9 alkoxides.

First, the adsorption behavior of linear nonene species was characterized by static DFT calculations. The resulting adsorption free energies at 350 °C for the *n*-nonene π-complexes and 2-nonyl carbenium ion in both zeolites are plotted in Figure 6. The adsorption enthalpies are shown in Figure S15. In MFI, the adsorbates are located in the straight 10-ring channel. In MOR-1—with the acid site located at the T1 position—the adsorbates are located in the main 12-ring channel. In MOR-2—with the acid site located at the T2 position—the adsorbates are located in the side pocket with the tail of the alkyl chain protruding in the main channel. Figure S16 shows the geometries of the optimized 1-nonene and 4-nonene π-complexes in both zeolites. In MFI, the adsorption free energies are found to be ca. 20−30 kJ·mol^{-1} lower than in MOR, which may be explained by the enhanced stabilization of the alkenes in the more confined 10-ring channels of MFI. The homologous *n*-nonene series has nearly equal adsorption free energies in MOR-1. However, in MOR-2, the adsorption free energy increases significantly from 1-nonene to 4-nonene. For 1-nonene only the double bond is situated in the side pocket, while for 4-nonene the alkyl chain penetrates much deeper into the 8-ring side pocket, thus resulting in an entropically less favorable configuration.

The 2-nonyl carbenium ion has a much lower adsorption strength than the nonene π-complex in both zeolites. The free energy difference between 1-nonene and the 2-nonyl carbenium ion is higher in MOR-1 (49 kJ·mol^{-1}) than in MFI (44 kJ·mol^{-1}), although it should be noted that this rather subtle difference lies within the margin of error. In MOR-2, the chemisorbed carbocation could not be localized as a stable state on the potential energy surface. Due to the proximity of

DOI: 10.1021/acscatal.9b01466
ACS Catal. 2019, 9, 6320−6334

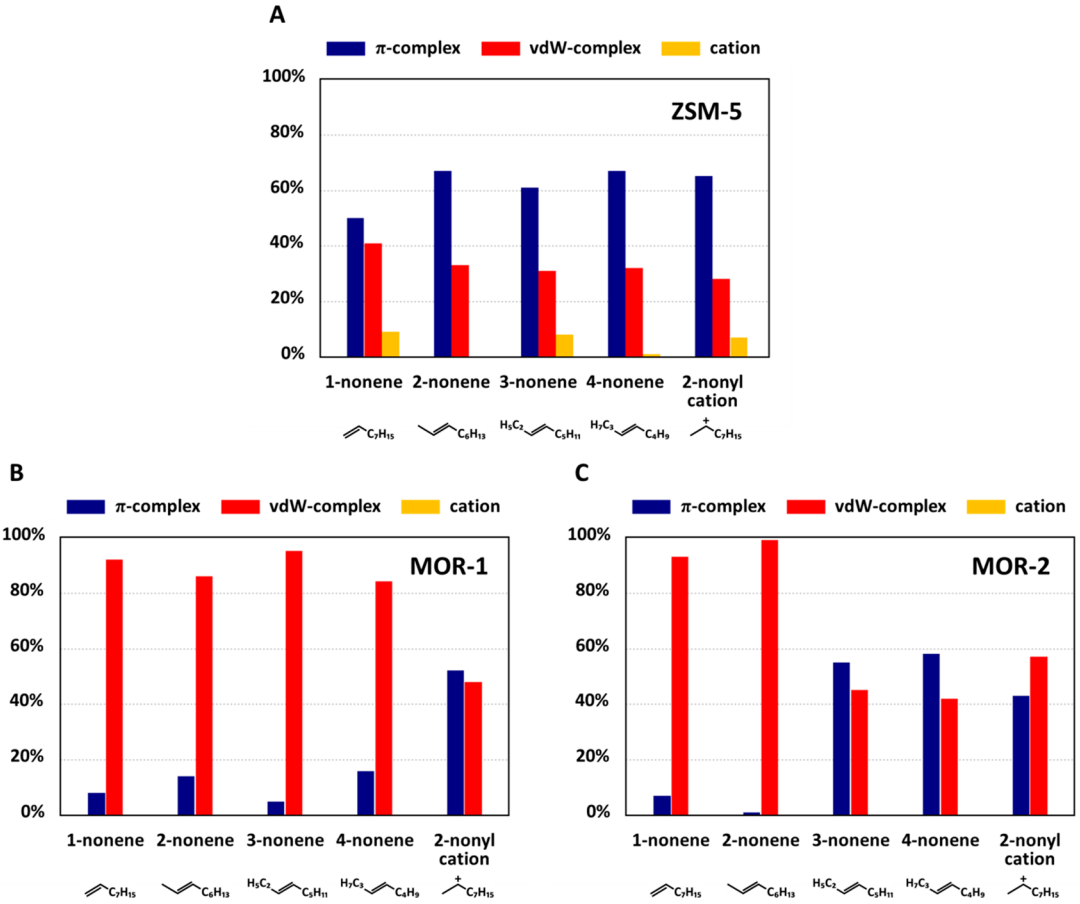

Figure 7. Sampling percentage of the π-complex, vdW-complex, and carbocation intermediates during the 100 ps MD simulations of the linear C_9 species at 350 °C in (A) H-ZSM-5, (B) H-MOR-1, and (C) H-MOR-2 (level of theory: revPBE-D3/DZVP-GTH).

the acid site in the side pocket, the 2-nonyl carbenium ion spontaneously deprotonates during the geometry optimization. In general, secondary carbenium ions are not expected to be very stable based on static calculations, as was also shown in our earlier work.[49,69]

From these static simulations, we can already conclude that C_9 alkenes generally adsorb more strongly in ZSM-5 compared to MOR. However, such static calculations show some limitations to properly account for the operating conditions. More particularly, only a single configuration of the adsorbate is considered, whereas at finite temperature, the adsorbed alkenes will typically possess sufficient energy to allow rapid rearrangements to other configurations.[49,69−72] To properly account for finite temperature effects and the configurational freedom of the guest species, MD simulations were performed at the reaction temperature of 350 °C.

The dynamic behavior of the C_9 species inside ZSM-5, MOR-1, and MOR-2 was evaluated through five simulations, starting from 1-nonene, 2-nonene, 3-nonene, and 4-nonene π-complexes and a 2-nonyl carbenium ion geometry. Compared to those in smaller alkenes, nonyl carbenium ions may be formed more easily because the charge-stabilizing inductive effect is more pronounced for longer chains.[49] Indeed, alkene (de)protonation reactions can occur in the course of the simulations as well as regular transitions between the alkene π-complex and vdW-complex. To distinguish between the different adsorption states at each instant, an empirical criterion based on characteristic distances was established, as described in ref 69.

Figure 7 shows the sampled π-complex, vdW-complex, and carbenium ion time fractions during the 100 ps MD simulations. As the simulation length is probably too short to satisfy the ergodic hypothesis, these results should be considered as a qualitative description of the stability of these intermediates. Furthermore, the applied level of theory might also influence the relative lifetimes of the various species. In H-ZSM-5, the π-complex is the most sampled state, irrespective of the starting configuration, followed by the vdW-complex and the carbocation (Figure 7A). In H-MOR-1, the weaker π-H interactions are not strong enough to compensate for the entropic gain of forming vdW-complexes at 350 °C. As a result, the vdW-complex is by far the most stable state, despite the easy accessibility of the active site (Figure 7B). In H-MOR-2, the lifetime of the physisorbed states depends on the position of the nonene species. When (partly) residing in the 8MR side pocket, π-complexes are quite stable due to the proximity of the acid site and the hindered mobility of the alkyl chain. When they reside in the main channel, the situation resembles H-MOR-1, and vdW-complexes are the most stable state (Figure 7C). In general, the π-complex fraction has a higher probability to occur in ZSM-5 than in MOR, which suggests that nonene will bind more strongly to the acid site in ZSM-5 at 350 °C.

To obtain further insight into the mobility of the nonene species in the zeolite pores in depth, 2D scatter plots of the mobility of 1-nonene and 4-nonene along the channel directions of MFI (Figure S17) and MOR (Figure S18) were constructed. In MOR-1, it is immediately clear that the alkene

DOI: 10.1021/acscatal.9b01466
ACS Catal. 2019, 9, 6320−6334

species can easily diffuse away from the active site along the large 12-ring main channel during the 100 ps simulation. In MOR-2, all nonene species diffuse rapidly from their initial position in the side pocket to the main channel, as this will result in a significant increase in conformational freedom. For 1-nonene the diffusion is almost instantaneous, while 4-nonene—which has a large part of the alkyl chain protruding in the side pocket—resides much longer in the side pocket before eventually traveling to the main channel, as evidenced by the large volume fraction of the side pocket which is visited during the simulation. The diffusion process to the main channel takes much longer, thus explaining the large π-complex fraction for the 3-nonene and 4-nonene simulations (Figure 7C). Also, 4-nonene and 3-nonene first undergo a spontaneous isomerization into 2-nonene before diffusing to the main channel, which confirms the higher adsorption strength of 2-nonene in MOR-2 as predicted by our static calculations (vide supra). On the other hand, in ZSM-5, the nonene species travel over a distance of only 10 Å along the straight channel. The C_9 alkenes are more tightly bound in ZSM-5 and remain adsorbed at the channel intersection. The tail of the alkyl chain can reside both in the straight and in the sinusoidal channel. For 4-nonene, these two preferred adsorption locations can clearly be distinguished from the adsorbate mobility (see Figure S17B).

In ZSM-5, transitions between the neutral alkene and the carbenium ion are observed in four out of the five simulations (Figure 7A). The total sampling time of the carbocation state ranges between 0 and 10 ps. Although carbenium ions are clearly much less stable than physisorbed alkenes, their lifetime is not negligible. In contrast, in both MOR zeolites, carbenium ions were not sampled, except for a very brief instant (<0.1 ps) during the double bond isomerizations. Even when starting from a carbenium ion configuration, immediate deprotonations occurred. These observations indicate that the relative energy difference between a nonyl carbenium ion and a physisorbed nonene is larger for MOR than for ZSM-5. The varying pore topology of both zeolites may explain the difference in carbocation stability. The size of the zeolite pores was previously shown to crucially affect the stability of alkene intermediates.[73−79] The 10-ring channels of ZSM-5 provide a much better confinement than the larger 12-ring channels of MOR. Furthermore, the location of the acid site at the channel intersection allows for an optimal accessibility. In the main channel of MOR, the average distance of the adsorbate to the zeolite wall will be larger than in ZSM-5. Therefore, the stabilizing effect of dispersion and vdW interactions will be reduced. In the 8-ring side pocket of MOR, a much more confined space is available for the adsorbate. However, this beneficial effect is counteracted by the overall mobility and entropy loss when the adsorbate is located in the side pocket.

Based on this qualitative data set, it can be concluded that carbenium ions seem to be formed preferentially on ZSM-5. However, to estimate the reactivity toward double bond activation, US simulations were carried out to reconstruct the free energy profile for the protonation of 1-nonene into a nonyl carbenium ion. In this way, the configurational freedom of the adsorbed C_9 species is equally well accounted for along the entire reaction coordinate. Figure S19 displays the resulting free energy profile for ZSM-5 and MOR-1 at 350 °C. Due to the tendency of nonene to diffuse along the main channel, zeolite MOR-2 was not considered. In ZSM-5, a free energy barrier of 61 kJ·mol^{-1} is obtained, while MOR-1 shows a protonation barrier of 67 kJ·mol^{-1}. The free energy difference between 1-nonene and a nonyl carbenium ion amounts to 32 and 42 kJ·mol^{-1}, respectively. Compared to the neutral alkene, carbenium ions are thus less stable in MOR than in ZSM-5 and their formation is slightly more highly activated. These free energy profiles clearly show the subtle difference between the two zeolites for the activation of 1-nonene.

The stability of carbenium ions is influenced not only by topology but, among others, also by temperature, chain length, and branching.[49,69] For higher reaction temperatures, it can be expected that the stability of carbenium ions will increase also in MOR. Furthermore, branching affects the stability of alkene intermediates to a large extent, since more stable tertiary carbenium ions may be formed upon protonation. Herein, we assumed that the importance of branched alkenes is limited, as linear α-olefins are the primary FTS products. However, the relevance of branched intermediates might be a topic for further investigation.

DISCUSSION

In line with previous reports,[7,8,16−20] our results confirm that the addition of a highly acidic zeolite to a CO_2 hydrogenation catalyst shifts the product distribution, breaking now the ASF distribution. The addition of highly acidic ZSM-5 enhances the formation of aromatics (see Figure 2A), increasing the selectivity to 61.4% in the liquid fraction (C_{5+}). However, this increase in aromatics is accompanied by a decrease of the C_2-C_{10} olefins and the formation of isobutane as the main byproduct (see Figure 3B). The addition of MOR enhances the formation of ethylene and propylene (see Figure 2B), with a total selectivity to ethylene of 11.5% and a total selectivity to propylene of 12.5%. However, in this zeolite, the bulk of the hydrocarbon fraction remains practically unchanged. Interestingly, the CO selectivity decreases in both cases (as low as 12.8% in the ZSM-5 and 13.7% in the MOR), implying that CO plays a role in both zeolitic reaction networks.[54] Furthermore, when CO is co-fed in the system, the carbon conversion and both aromatic and light olefin selectivities sharply increase (Table 1).

The proximity of the two components of the bifunctional catalyst was found to be critical: when the spatial arrangement was changed from dual bed to mortar mixed, the main product was always CO for both MOR and ZSM-5 (see Figure S7). These results can be a consequence of K poisoning by the acidity of the zeolite.[8] The SiO_2/Al_2O_3 ratio was also found to be critical for the ZSM-5 system: upon increasing the SiO_2/Al_2O_3 ratio, the total aromatic selectivity decreased, showing a linear relationship between the aromatics produced and the paraffins formed as byproducts (see Figure 3B). According to our results, for each mole of aromatics produced, 0.9 mol of C_3 paraffins and 1.5 mol of C_4 paraffins are co-produced, regardless of the SiO_2/Al_2O_3 ratio.

To unravel this complicated reaction network, advanced MAS ssNMR spectroscopy, including 2D correlation experiments ($^1H-^{13}C$ and $^{13}C-^{13}C$), was performed on the post-reacted zeolite materials to derive structural information on trapped organics. Altogether, our ssNMR study indicates that methylated olefinic/vinylic species, zeolite surface formate species, and paraffins were primarily trapped on the post-reacted MOR zeolite (Figure 4), whereas post-reacted zeolite ZSM-5 was overwhelmed by alkylated (i.e., both methylated and ethylated) aromatics, polyaromatics, and olefinic/vinylic species as well as paraffins (Figure 5 and Figure S12). The 2D $^{13}C-^{13}C$ spectrum also illuminates the presence of surface-

DOI: 10.1021/acscatal.9b01466
ACS Catal. 2019, 9, 6320−6334

adsorbed methanol and dimethyl ether, as well as surface methoxy species on the post-reacted zeolite ZSM-5 material. Therefore, the dominating reaction intermediates in the present case were characteristically similar to the hydrocarbon pool (HCP) species, like in the MTH process.[56]

By combining static DFT calculations and advanced MD simulations, the difference in adsorption behavior and reactivity of C_9 alkene intermediates between ZSM-5 and MOR was clarified. The free energy profile for 1-nonene adsorption and protonation at 350 °C is schematically represented in Figure 8. The protonation barrier referenced

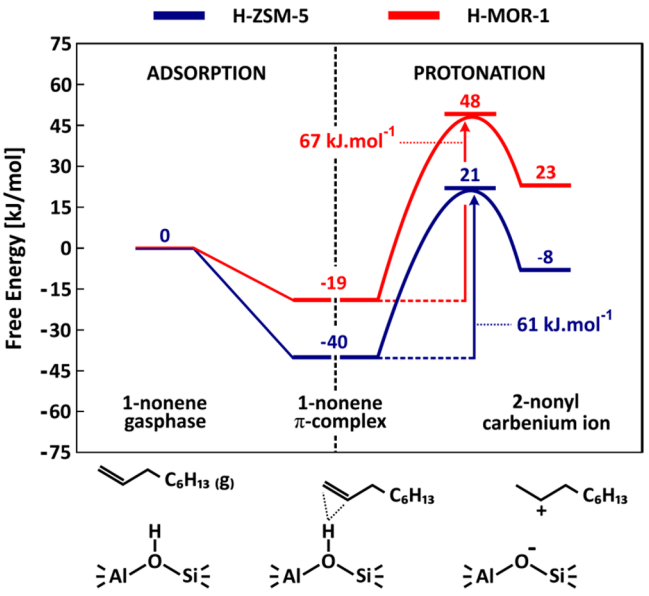

Figure 8. Free energy profile for the adsorption (from static calculations, level of theory: PBE-D3) and protonation (from umbrella sampling, level of theory: revPBE-D3/TZVP-GTH) of 1-nonene π-complex into 2-nonyl carbenium ion in H-ZSM-5 (blue) and H-MOR-1 (red) at 350 °C, with the empty framework and 1-nonene in gas phase as reference states.

to the empty framework and 1-nonene in the gas phase is 27 kJ·mol^{-1} higher in MOR than in ZSM-5. Compared to the gas-phase reactants, the nonyl carbenium ion is stabilized by 8 kJ·mol^{-1} in ZSM-5 and destabilized by 23 kJ·mol^{-1} in MOR. It should be stressed that the adsorption free energies were obtained from static calculations, whereas the activation free energies were obtained from MD simulations. As a result, the absolute quantitative values may be prone to some uncertainties. However, the overall data set illustrates the difference in carbenium ion stability for both zeolites. The reason for this reactivity difference is two-fold. First, 1-nonene adsorbs less strongly on MOR, which may be explained by the reduced confinement of the large 12MR zeolite channels compared to ZSM-5. Furthermore, it was discovered that nonene species tend to diffuse into the main channel in MOR, even when they were originally located in the side pocket. Second, the intrinsic activation barrier for the protonation of 1-nonene is slightly higher in H-MOR.

The different product distributions obtained from the two catalysts can (partly) be attributed to the ability of these zeolites to activate alkenes and form carbenium ions. Carbenium ions indeed play a crucial role in the further conversion of large olefins into either aromatics, light olefins, or alkanes. By properly choosing the zeolite topology, the stabilization of the involved intermediates can be influenced and the selectivity can be tuned toward the targeted product distribution. In ZSM-5, the 10-ring channels of ZSM-5 provide a much better confinement than the larger 12-ring channels of MOR, in agreement with earlier studies which showed the importance of the channel confinement in stabilizing small alkane intermediates.[80] In addition, ZSM-5 can more easily activate long alkenes to form carbenium ions that can further be incorporated into the aromatization cycle. On the other hand, in MOR the protonation barrier is higher and, as consequence, the bulk of the heavy olefin fraction remains practically unchanged (Figure 2B). Furthermore, since the accessible Brønsted acid sites of MOR may be blocked by $K(H_2O)_8^+$ (Figure S13), it could not be expected to facilitate the aromatization of olefins, and indeed, no aromatics species were evidenced by ssNMR on MOR (unlike H-ZSM-5).

Based on the aforementioned results, a catalytic pathway for the Fe_2O_3@KO_2/zeolite-catalyzed hydrogenation of CO_2 to hydrocarbons is proposed in Figure 9. First, Fe_2O_3@KO_2 catalyzes the RWGS reaction to produce CO and water from the reaction mixture (CO_2 + H_2) (Figure 9A). Next, part of the CO is transformed in the Fe nanoparticles to produce the whole range of hydrocarbons (see Table S4) while the remaining CO diffuses to the confined pores of both MOR and ZSM-5 zeolites to produce surface formate species, which are subsequently hydrogenated to form SMS in situ[20] (Figure 9B). This SMS species undergoes several transformations, yielding mostly ethylene. It is worth mentioning that the mechanism of formation of olefins directly from the surface carbonylated species has recently been elucidated,[55] which presumably goes through the formation of a ketene-based reaction intermediate during both MTH and syngas chemistry over zeolite.[81] Finally, the olefins produced on the Fe_2O_3@KO_2 catalyst plus the ones resulting from the SMS species are further incorporated into the aromatization cycle. This cycle takes place exclusively on ZMS-5 and greatly depends on the acidity of the zeolite (Figure 3A). In addition, for each aromatic formed, paraffins are also produced,[14,54] with isobutane as the main byproduct (Figure 3B). Furthermore, the initial aromatics can undergo several transformations (i.e., transalkylation, isomerization), widening the final aromatic product distribution (Figure S6).

Last but not least, the C_2−C_4 olefin STY of the Fe_2O_3@KO_2/MOR composite and the aromatic STY of the Fe_2O_3@KO_2/ZSM-5 composite reported here turns out to be the highest of those for the existing bifunctional systems[7,8,16−20,82−90] (see Figures S20 and S21 and Table S1). These elevated conversions can be attributed to the optimal performance of the Fe_2O_3@KO_2 stand-alone catalyst[21] and the addition of the correct zeolite that enables the selectivity increase to either light olefins (MOR) or aromatics (ZSM-5).

CONCLUSIONS

The combination in one single reactor of the appropriate Fe catalyst and zeolite topology results in the conversion of CO_2 to olefins and aromatics with high selectivity and unprecedented values of productivity. Product distribution can be easily shifted to either light olefins (in case of MOR) or aromatics (in case of ZSM-5) by selecting the appropriate zeolite. Furthermore, the presence of a zeolite enables the conversion of undesired CO, boosting the total selectivity to the desired hydrocarbon fraction. Solid-state nuclear magnetic resonance characterization of the spent zeolites revealed that for both zeolites the reaction mechanism is driven by the

DOI: 10.1021/acscatal.9b01466
ACS Catal. 2019, 9, 6320−6334

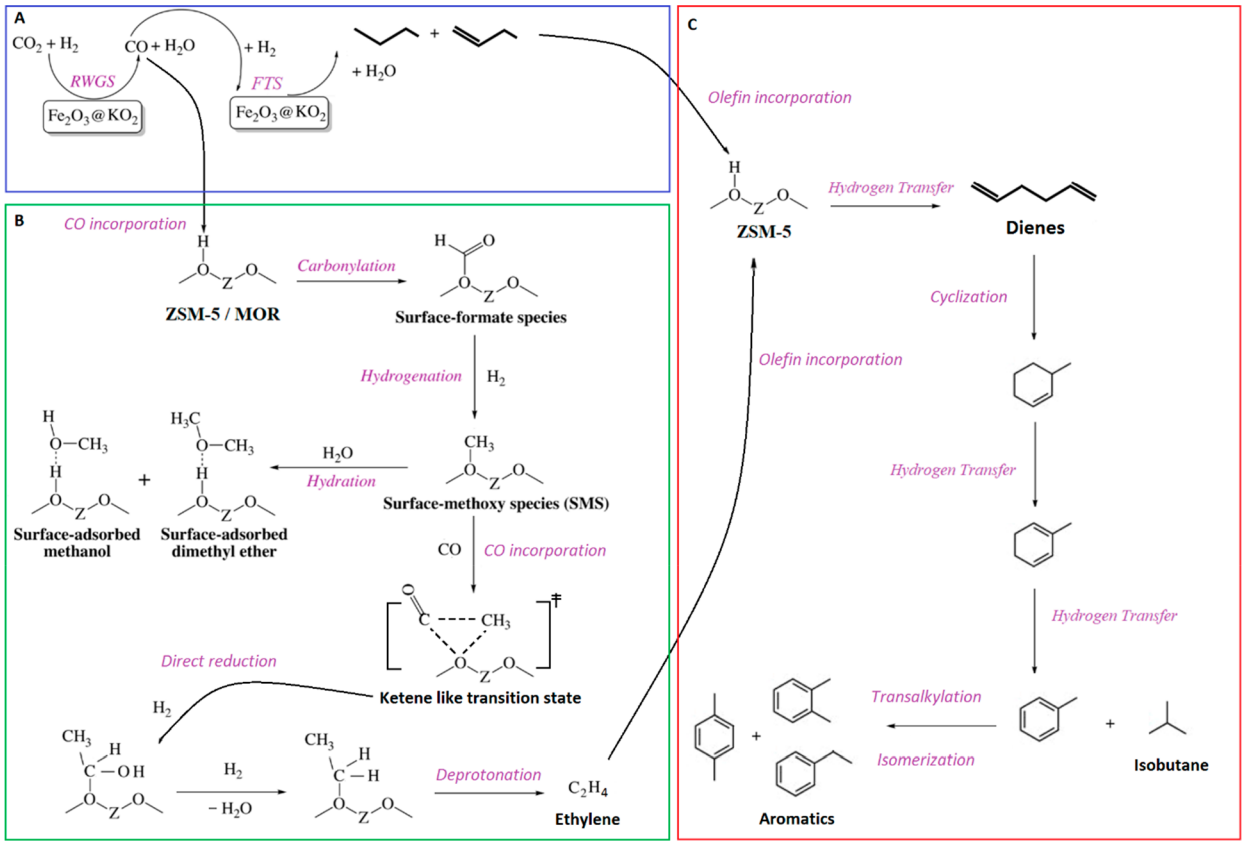

Figure 9. Proposed reaction pathways of the $Fe_2O_3@KO_2$/zeolite-catalyzed hydrogenation of CO_2 to light olefins and aromatics. (A) CO_2 hydrogenation pathway on the stand-alone $Fe_2O_3@KO_2$ catalyst. (B) CO incorporation pathway on MOR and ZMS-5. (C) Aromatization pathway on ZSM-5.

incorporation of CO in the network in the form of surface formate. A combined static and dynamic set of DFT simulations showed a higher potential of ZSM-5 to activate long alkenes toward carbenium ions, in contrast to MOR where these fractions are nearly unreactive. This explains the higher selectivity of ZSM-5 toward formation of aromatics. Our findings could help unravel the reaction network in bifunctional systems with the ultimate goal of the mass adoption of non-fossil-fuel technologies for the production of hydrocarbons in the near future.

■ ASSOCIATED CONTENT

Supporting Information

The Supporting Information is available free of charge on the ACS Publications website at DOI: 10.1021/acscatal.9b01466.

Comparison with state-of-the-art materials, additional computational calculations, characterization of catalysts, and complementary activity measurements, including Figures S1−S21 and Tables S1−S5 (PDF)

■ AUTHOR INFORMATION

Corresponding Authors

*E-mail: veronique.vanspeybroeck@ugent.be.
*E-mail: jorge.gascon@kaust.edu.sa.

ORCID

Abhishek Dutta Chowdhury: 0000-0002-4121-7375
Samy Ould-Chikh: 0000-0002-3486-0944
Veronique van Speybroeck: 0000-0003-2206-178X
Jorge Gascon: 0000-0001-7558-7123

Notes

The authors declare no competing financial interest.

■ ACKNOWLEDGMENTS

Funding for this work was provided by King Abdullah University of Science and Technology (KAUST). V.V.S. and P.C. acknowledge funding from the European Union's Horizon 2020 research and innovation program (consolidator ERC grant agreement no. 647755-DYNPOR (2015−2020)). K.D.W. is a fellow funded by the FWO (FWO16-PDO-047). Dr. Vanduyfhuys is acknowledged for his contribution to constructing the mobility plots. The computational resources and services used were provided by Ghent University (Stevin Supercomputer Infrastructure), the VSC (Flemish Supercomputer Center), funded by the Research Foundation - Flanders (FWO).

■ REFERENCES

(1) WMO. *The State of Greenhouse Gases in the Atmosphere Based on Global Observations through 2016*, Greenhouse Gas Bulletin (GHG Bulletin) No. 13; World Meteorological Organization, 2017.
(2) Global Carbon Budget 2018. https://www.globalcarbonproject.org/carbonbudget (accessed May 25, 2019).
(3) Alper, E.; Orhan, O. Y. CO_2 utilization: Developments in conversion processes. *Petroleum* **2017**, 3, 109−126.
(4) Álvarez, A.; Bansode, A.; Urakawa, A.; Bavykina, A. V.; Wezendonk, T. A.; Makkee, M.; Gascon, J.; Kapteijn, F. Challenges in the Greener Production of Formates/Formic Acid, Methanol, and

DOI: 10.1021/acscatal.9b01466
ACS Catal. 2019, 9, 6320−6334

DME by Heterogeneously Catalyzed CO_2 Hydrogenation Processes. *Chem. Rev.* **2017**, *117*, 9804−9838.
(5) Centi, G.; Quadrelli, E. A.; Perathoner, S. Catalysis for CO_2 conversion: a key technology for rapid introduction of renewable energy in the value chain of chemical industries. *Energy Environ. Sci.* **2013**, *6*, 1711−1731.
(6) Dokania, A.; Ramirez, A.; Bavykina, B.; Gascon, J. Heterogeneous Catalysis for the Valorization of CO_2: Role of Bifunctional Processes in the Production of Chemicals. *ACS Energy Lett.* **2019**, *4*, 167−179.
(7) Gao, P.; Dang, S.; Li, S.; Bu, X.; Liu, Z.; Qiu, M.; Yang, C.; Wang, H.; Zhong, L.; Han, Y.; Liu, Q.; Wei, W.; Sun, Y. Direct Production of Lower Olefins from CO_2 Conversion via Bifunctional Catalysis. *ACS Catal.* **2018**, *8*, 571−578.
(8) Wei, J.; Ge, Q.; Yao, R.; Wen, Z.; Fang, C.; Guo, L.; Xu, H.; Sun, J. Directly converting CO_2 into a gasoline fuel. *Nat. Commun.* **2017**, *8*, 15174.
(9) Ramirez, A.; Gevers, L.; Bavykina, A.; Ould-Chikh, S.; Gascon, J. Metal Organic Framework-Derived Iron Catalysts for the Direct Hydrogenation of CO_2 to Short Chain Olefins. *ACS Catal.* **2018**, *8*, 9174−9182.
(10) Rahimi, N.; Karimzadeh, R. Catalytic Cracking of Hydrocarbons over Modified ZSM-5 Zeolites to Produce Light Olefins: A Review. *Appl. Catal., A* **2011**, *398*, 1−17.
(11) Jadhav, S. G.; Vaidya, P. D.; Bhanage, B. M.; Joshi, J. B. Catalytic Carbon Dioxide Hydrogenation to Methanol: A Review of Recent Studies. *Chem. Eng. Res. Des.* **2014**, *92*, 2557−2567.
(12) Yarulina, I.; De Wispelaere, K.; Bailleul, S.; Goetze, J.; Radersma, M.; Abou-Hamad, E.; Vollmer, I.; Goesten, M.; Mezari, B.; Hensen, E. J. M.; Martínez-Espín, J. S.; Morten, M.; Mitchell, S.; Perez-Ramirez, J.; Olsbye, O.; Weckhuysen, B. M.; Van Speybroeck, V.; Kapteijn, F.; Gascon, J. Structure-Performance Descriptors and the Role of Lewis Acidity in the Methanol-to-Propylene Process. *Nat. Chem.* **2018**, *10*, 804−812.
(13) Yarulina, I.; Dutta Chowdhury, A.; Meirer, F.; Weckhuysen, B. M.; Gascon, J. Recent Trends and Fundamental insights in the Methanol-to-Hydrocarbons Process. *Nat. Catal.* **2018**, *1*, 398−411.
(14) Batchu, R.; Galvita, V. V.; Alexopoulos, K.; Van der Borght, K.; Poelman, H.; Reyniers, M.-F.; Marin, G. B. Role of Intermediates in Reaction Pathways from Ethene to Hydrocarbons over H-ZSM-5. *Appl. Catal., A* **2017**, *538*, 207−220.
(15) Guisnet, M.; Gnep, N. S. Mechanism of Short-Chain Alkane Transformation over Protonic Zeolites. Alkylation, Disproportionation and Aromatization. *Appl. Catal., A* **1996**, *146*, 33−64.
(16) Gao, J.; Jia, C.; Liu, B. Direct and Selective Hydrogenation of CO_2 to Ethylene and Propene by Bifunctional Catalysts. *Catal. Sci. Technol.* **2017**, *7*, 5602−5607.
(17) Liu, X.; Wang, M.; Zhou, C.; Zhou, W.; Cheng, K.; Kang, J.; Zhang, Q.; Deng, W.; Wang, Y. Selective Transformation of Carbon Dioxide into Lower Olefins with a Bifunctional Catalyst Composed of $ZnGa_2O_4$ and SAPO-34. *Chem. Commun.* **2018**, *54*, 140−143.
(18) Li, Z.; Wang, J.; Qu, Y.; Liu, H.; Tang, C.; Miao, S.; Feng, Z.; An, H.; Li, C. Highly Selective Conversion of Carbon Dioxide to Lower Olefins. *ACS Catal.* **2017**, *7*, 8544−8548.
(19) Dang, S.; Gao, P.; Liu, Z.; Chen, X.; Yang, C.; Wang, H.; Zhong, L.; Li, S.; Sun, Y. Role of Zirconium in Direct CO_2 Hydrogenation to Lower Olefins on Oxide/Zeolite Bifunctional Catalysts. *J. Catal.* **2018**, *364*, 382−393.
(20) Ni, Y.; Chen, Z.; Fu, Y.; Liu, Y.; Zhu, W.; Liu, Z. Selective Conversion of CO_2 and H_2 into Aromatics. *Nat. Commun.* **2018**, *9*, 3457.
(21) Ramirez, A.; Ould-Chikh, S.; Gevers, L.; Dutta Chowdhury, A.; Abou-hamad, E.; Aguilar-Tapia, A.; Hazemann, J.; Wehbe, N.; Al Abdulghani, A. J.; Kozlov, S. M.; Cavallo, L.; Gascon, J. Tandem Conversion of CO_2 to Valuable Hydrocarbons in Highly Concentrated Potassium Iron Catalysts. *ChemCatChem* **2019**, DOI: 10.1002/cctc.201900762.
(22) Ono, Y. Transformation of Lower Alkanes into Aromatic Hydrocarbons over ZSM-5 Zeolites. *Catal. Rev.: Sci. Eng.* **1992**, *34*, 179−226.
(23) Jiao, F.; Pan, X.; Gong, K.; Chen, Y.; Li, G.; Bao, X. Shape-Selective Zeolites Promote Ethylene Formation from Syngas via a Ketene Intermediate. *Angew. Chem., Int. Ed.* **2018**, *57*, 4692.
(24) Jiao, F.; Li, J.; Pan, X.; Xiao, J.; Li, H.; Ma, H.; Wei, M.; Pan, Y.; Zhou, Z.; Li, M.; Miao, S.; Li, J.; Zhu, Y.; Xiao, D.; He, T.; Yang, J.; Qi, F.; Fu, Q.; Bao, X. Selective conversion of syngas to light olefins. *Science* **2016**, *351*, 1065−1068.
(25) Van Speybroeck, V.; De Wispelaere, K.; Van der Mynsbrugge, J.; Vandichel, M.; Hemelsoet, K.; Waroquier, M. First principle chemical kinetics in zeolites: the methanol-to-olefin process as a case study. *Chem. Soc. Rev.* **2014**, *43*, 7326−7357.
(26) International Zeolite Association Home Page, http:www.iza-online.org (accessed May 25, 2019).
(27) Van Speybroeck, V.; Hemelsoet, K.; Joos, L.; Waroquier, M.; Bell, R. G.; Catlow, C. R. A. Advances in theory their application within the field of zeolite chemistry. *Chem. Soc. Rev.* **2015**, *44*, 7044−7111.
(28) Kresse, G.; Hafner, J. Ab initio molecular dynamics for liquid metals. *Phys. Rev. B: Condens. Matter Mater. Phys.* **1993**, *47*, 558−561.
(29) Kresse, G.; Hafner, J. Ab initio molecular-dynamics simulation of the liquid-metal amorphous-semiconductor transition in germanium. *Phys. Rev. B: Condens. Matter Mater. Phys.* **1994**, *49*, 14251−14269.
(30) Kresse, G.; Furthmüller, J. Efficiency of ab-initio total energy calculations for metals and semiconductors using a plane-wave basis set. *Comput. Mater. Sci.* **1996**, *6*, 15−50.
(31) Kresse, G.; Furthmüller, J. Efficient iterative schemes for ab initio total-energy calculations using a plane-wave basis set. *Phys. Rev. B: Condens. Matter Mater. Phys.* **1996**, *54*, 11169−11186.
(32) Perdew, J. P.; Burke, K.; Ernzerhof, M. Generalized Gradient Approximation Made Simple. *Phys. Rev. Lett.* **1996**, *77*, 3865−3868.
(33) Grimme, S.; Antony, J.; Ehrlich, S.; Krieg, H. A consistent and accurate ab initio parametrization of density functional dispersion correction (DFT-D) for the 94 elements H-Pu. *J. Chem. Phys.* **2010**, *132*, 154104.
(34) Kresse, G.; Joubert, D. From ultrasoft pseudopotentials to the projector augmented-wave method. *Phys. Rev. B: Condens. Matter Mater. Phys.* **1999**, *59*, 1758−1775.
(35) Blöchl, P. E. Projector augmented-wave method. *Phys. Rev. B: Condens. Matter Mater. Phys.* **1994**, *50*, 17953−17979.
(36) Ghysels, A.; Van Neck, D.; Waroquier, M. Cartesian formulation of the mobile block Hessian approach to vibrational analysis in partially optimized systems. *J. Chem. Phys.* **2007**, *127*, 164108.
(37) Reetz, M. T.; Meiswinkel, A.; Mehler, G.; Angermund, K.; Graf, M.; Thiel, W.; Mynott, R.; Blackmond, D. G. Why Are BINOL-Based Monophosphites Such Efficient Ligands in Rh-Catalyzed Asymmetric Olefin Hydrogenation? *J. Am. Chem. Soc.* **2005**, *127*, 10305−10313.
(38) Donoghue, P. J.; Helquist, P.; Norrby, P. O.; Wiest, O. Development of a Q2MM Force Field for the Asymmetric Rhodium Catalyzed Hydrogenation of Enamides. *J. Chem. Theory Comput.* **2008**, *4*, 1313−1323.
(39) Ghysels, A.; Verstraelen, T.; Hemelsoet, K.; Waroquier, M.; Van Speybroeck, V. TAMkin: A Versatile Package for Vibrational Analysis and Chemical Kinetics. *J. Chem. Inf. Model.* **2010**, *50*, 1736−1750.
(40) Van de Vondele, J.; Krack, M.; Mohamed, F.; Parrinello, M.; Chassaing, T.; Hutter, J. QUICKSTEP: Fast and accurate density functional calculations using a mixed Gaussian and plane waves approach. *Comput. Phys. Commun.* **2005**, *167*, 103−128.
(41) Yang, K.; Zheng, J.; Zhao, Y.; Truhlar, D. G. Tests of the RPBE, revPBE, τ-HCTHhyb, ωB97X-D, and MOHLYP density functional approximations and 29 others against representative databases for diverse bond energies and barrier heights in catalysis. *J. Chem. Phys.* **2010**, *132*, 164117.

DOI: 10.1021/acscatal.9b01466
ACS Catal. 2019, 9, 6320−6334

(42) Goedecker, S.; Teter, M.; Hutter, J. Separable dual-space Gaussian pseudopotentials. *Phys. Rev. B: Condens. Matter Mater. Phys.* **1996**, *54*, 1703−1710.
(43) Lippert, G.; Hutter, J.; Parrinello, M. The Gaussian and augmented-plane-wave density functional method for ab initio molecular dynamics simulations. *Theor. Chem. Acc.* **1999**, *103*, 124−140.
(44) Lippert, G.; Hutter, J.; Parrinello, M. A hybrid Gaussian and plane wave density functional scheme. *Mol. Phys.* **1997**, *92*, 477−488.
(45) Nosé, S. A molecular dynamics method for simulations in the canonical ensemble. *Mol. Phys.* **1984**, *52*, 255−268.
(46) Martyna, G. J.; Klein, M. L.; Tuckerman, M. Nosé-Hoover chains: The canonical ensemble via continuous dynamics. *J. Chem. Phys.* **1992**, *97*, 2635−2643.
(47) Martyna, G. J.; Tobias, D. J.; Klein, M. L. Constant pressure molecular dynamics algorithms. *J. Chem. Phys.* **1994**, *101*, 4177−4189.
(48) Tribello, G. A.; Bonomi, M.; Branduardi, D.; Camilloni, C.; Bussi, G. PLUMED 2: New feathers for an old bird. *Comput. Phys. Commun.* **2014**, *185*, 604−613.
(49) Cnudde, P.; De Wispelaere, K.; Vanduyfhuys, L.; Demuynck, R.; Waroquier, M.; Van Speybroeck, V.; Van der Mynsbrugge, J. How Chain Length and Branching Influence the Alkene Cracking Reactivity on H-ZSM-5. *ACS Catal.* **2018**, *8*, 9579−9595.
(50) Kästner, J. Umbrella sampling. *WIREs Comput. Mol. Sci.* **2011**, *1*, 932−942.
(51) Kumar, S.; Rosenberg, J. M.; Bouzida, D.; Swendsen, R. H.; Kollman, P. A. The weighted histogram analysis method for free-energy calculations on biomolecules. I. The method. *J. Comput. Chem.* **1992**, *13*, 1011−1021.
(52) Souaille, M.; Roux, B. Extension to the weighted histogram analysis method: combining umbrella sampling with free energy calculations. *Comput. Phys. Commun.* **2001**, *135*, 40−57.
(53) Cheng, K.; Zhou, W.; Kang, J.; He, S.; Shi, S.; Zhang, Q.; Pan, Y.; Wen, W.; Wang, Y. Bifunctional Catalysts for One-Step Conversion of Syngas into Aromatics with Excellent Selectivity and Stability. *Chem.* **2017**, *3*, 334−347.
(54) Guisnet, M.; Gnep, N. S.; Alario, F. Aromatization of short chain alkanes on zeolite catalysts. *Appl. Catal., A* **1992**, *89*, 1−30.
(55) Dutta Chowdhury, A.; Paioni, A. L.; Houben, K.; Whiting, G. T.; Baldus, M.; Weckhuysen, B. M. Bridging the Gap between the Direct and Hydrocarbon Pool Mechanisms of the Methanol-to-Hydrocarbon Process. *Angew. Chem., Int. Ed.* **2018**, *57*, 8095−8099.
(56) Yarulina, I.; Dutta Chowdhury, A.; Meirer, F.; Weckhuysen, B. M.; Gascon, J. Recent Trends and Fundamental Insights in the Methanol-to-Olefins Process. *Nat. Catal.* **2018**, *1*, 398−411.
(57) Dutta Chowdhury, A.; Houben, K.; Whiting, G. T.; Mokhtar, M.; Asiri, A. M.; Al-Thabaiti, S. A.; Baldus, M.; Weckhuysen, B. M.; Basahel, S. N. Initial carbon-carbon bond formation during the early stages of the methanol-to-olefin process proven by zeolite-trapped acetate and methyl acetate. *Angew. Chem., Int. Ed.* **2016**, *55*, 15840−15845.
(58) Ristanović, Z.; Dutta Chowdhury, A.; Brogaard, R. Y.; Houben, K.; Baldus, M.; Hofkens, J.; Roeffaers, M. B. J.; Weckhuysen, B. M. Reversible and Site-Dependent Proton-Transfer in Zeolites Uncovered at the Single-Molecule Level. *J. Am. Chem. Soc.* **2018**, *140*, 14195−14205.
(59) Persson, I. Hydrated metal ions in aqueous solution: How regular are their structures? *Pure Appl. Chem.* **2010**, *82*, 1901−1917.
(60) Weitkamp, J. Catalytic Hydrocracking-Mechanisms and Versatility of the Process. *ChemCatChem* **2012**, *4*, 292−306.
(61) Kissin, Y. V. Chemical Mechanisms of Catalytic Cracking Over Solid Acidic Catalysts: Alkanes and Alkenes. *Catal. Rev.: Sci. Eng.* **2001**, *43*, 85−146.
(62) Martínez-Espín, J. S.; De Wispelaere, K.; Janssens, T. V. W.; Svelle, S.; Lillerud, K. P.; Beato, P.; Van Speybroeck, V.; Olsbye, U. Hydrogen Transfer versus Methylation: On the Genesis of Aromatics Formation in the Methanol-To-Hydrocarbons Reaction over H-ZSM-5. *ACS Catal.* **2017**, *7*, 5773−5780.
(63) Buchanan, J. S.; Santiesteban, J. G.; Haag, W. O. Mechanistic Considerations in Acid-Catalyzed Cracking of Olefins. *J. Catal.* **1996**, *158*, 279−287.
(64) Van Speybroeck, V.; De Wispelaere, K.; Van der Mynsbrugge, J.; Vandichel, M.; Hemelsoet, K.; Waroquier, M. First principle chemical kinetics in zeolites: the methanol-to-olefin process as a case study. *Chem. Soc. Rev.* **2014**, *43*, 7326−7357.
(65) Haag, W. O.; Lago, R. M.; Rodewald, P. G. Aromatics, light olefins and gasoline from methanol: Mechanistic pathways with ZSM-5 zeolite catalyst. *J. Mol. Catal.* **1982**, *17*, 161−169.
(66) Abbot, J.; Corma, A.; Wojciechowski, B. W. The catalytic isomerization of 1-hexene on H-ZSM-5 zeolite: The effects of a shape-selective catalyst. *J. Catal.* **1985**, *92*, 398−408.
(67) Abbot, J.; Wojciechowski, B. W. Catalytic cracking and skeletal isomerization of n-Hexene on ZSM-5 Zeolite. *Can. J. Chem. Eng.* **1985**, *63*, 451−461.
(68) Kissin, Y. V. Chemical Mechanism of Hydrocarbon Cracking over Solid Acidic Catalysts. *J. Catal.* **1996**, *163*, 50−62.
(69) Cnudde, P.; De Wispelaere, K.; Van der Mynsbrugge, J.; Waroquier, M.; Van Speybroeck, V. Effect of temperature and branching on the nature and stability of alkene cracking intermediates in H-ZSM-5. *J. Catal.* **2017**, *345*, 53−69.
(70) Hajek, J.; Van der Mynsbrugge, J.; De wispelaere, K.; Cnudde, P.; Vanduyfhuys, L.; Waroquier, M.; Van Speybroeck, V. On the stability and nature of adsorbed pentene in Brønsted acid zeolite H-ZSM-5 at 323 K. *J. Catal.* **2016**, *340*, 227−235.
(71) Bučko, T.; Benco, L.; Hafner, J.; Ángyán, J. G. Monomolecular cracking of propane over acidic chabazite: An ab initio molecular dynamics and transition path sampling study. *J. Catal.* **2011**, *279*, 220−228.
(72) Zimmerman, P. M.; Tranca, D. C.; Gomes, J.; Lambrecht, D. S.; Head-Gordon, M.; Bell, A. T. Ab Initio Simulations Reveal that Reaction Dynamics Strongly Affect Product Selectivity for the Cracking of Alkanes over H-MFI. *J. Am. Chem. Soc.* **2012**, *134*, 19468−19476.
(73) Gounder, R.; Iglesia, E. Catalytic Consequences of Spatial Constraints and Acid Site Location for Monomolecular Alkane Activation on Zeolites. *J. Am. Chem. Soc.* **2009**, *131*, 1958−1971.
(74) Gounder, R.; Iglesia, E. Effects of Partial Confinement on the Specificity of Monomolecular Alkane Reactions for Acid Sites in Side Pockets of Mordenite. *Angew. Chem., Int. Ed.* **2010**, *49*, 808−811.
(75) Sarazen, M. L.; Doskocil, E.; Iglesia, E. Catalysis on solid acids: Mechanism and catalyst descriptors in oligomerization reactions of light alkenes. *J. Catal.* **2016**, *344*, 553−569.
(76) Sarazen, M. L.; Iglesia, E. Stability of bound species during alkene reactions on solid acids. *Proc. Natl. Acad. Sci. U. S. A.* **2017**, *114*, E3900−E3908.
(77) De Moor, B. A.; Reyniers, M. F.; Gobin, O. C.; Lercher, J. A.; Marin, G. B. Adsorption of C2−C8 n-Alkanes in Zeolites. *J. Phys. Chem. C* **2011**, *115*, 1204−1219.
(78) Nguyen, C. M.; De Moor, B. A.; Reyniers, M. F.; Marin, G. B. Isobutene Protonation in H-FAU, H-MOR, H-ZSM-5, and H-ZSM-22. *J. Phys. Chem. C* **2012**, *116*, 18236−18249.
(79) Bučko, T.; Hafner, J. The role of spatial constraints and entropy in the adsorption and transformation of hydrocarbons catalyzed by zeolites. *J. Catal.* **2015**, *329*, 32−48.
(80) Janda, A.; Vlaisavljevich, B.; Lin, L. C.; Smit, B.; Bell, A. T. Effects of Zeolite Structural Confinement on Adsorption Thermodynamics and Reaction Kinetics for Monomolecular Cracking and Dehydrogenation of n-Butane. *J. Am. Chem. Soc.* **2016**, *138*, 4739−4756.
(81) Dutta Chowdhury, A.; Gascon, J. The Curious Case of Ketene in Zeolite Chemistry and Catalysis. *Angew. Chem., Int. Ed.* **2018**, *57*, 14982−14985.
(82) Kuei, C. K.; Lee, M. D. Hydrogenation of Carbon Dioxide by Hybrid Catalysts, Direct Synthesis of Aromatics from Carbon Dioxide and Hydrogen. *Can. J. Chem. Eng.* **1991**, *69*, 347−354.
(83) Fujiwara, M.; Ando, H.; Tanaka, M.; Souma, Y. Hydrogenation of Carbon Dioxide over Cu-Zn-Chromate/Zeolite Composite

DOI: 10.1021/acscatal.9b01466
ACS Catal. 2019, 9, 6320−6334

Catalyst: The Effects of Reaction Behavior of Alkenes on Hydrocarbon Synthesis. *Appl. Catal., A* **1995**, *130*, 105−116.
(84) Fujiwara, M.; Kieffer, R.; Ando, H.; Xu, Q.; Souma, Y. Change of Catalytic Properties of FeZnO/Zeolite Composite Catalyst in the Hydrogenation of Carbon Dioxide. *Appl. Catal., A* **1997**, *154*, 87−101.
(85) Kim, H.; Choi, D. H.; Nam, S. S.; Choi, M. J.; Lee, K. W. The Selective Synthesis of Lower Olefins (C_2 - C_4) by the CO_2 Hydrogenation over Iron Catalysts Promoted with Potassium and Supported on Ion Exchanged (H, K) Zeolite-Y. *Stud. Surf. Sci. Catal.* **1998**, *114*, 407−410.
(86) Xu, Q.; He, D.; Fujiwara, M.; Tanaka, M.; Matsumura, Y.; Souma, Y.; Ando, H.; Yamanaka, H. Hydrogenation of Carbon Dioxide over Fe-Cu-Na/Zeolite Composite Catalysts. *Stud. Surf. Sci. Catal.* **1998**, *114*, 423−426.
(87) Tan, Y.; Fujiwara, M.; Ando, H.; Xu, Q.; Souma, Y. Selective Formation of iso-Butane from Carbon Dioxide and Hydrogen over Composite Catalysts. *Stud. Surf. Sci. Catal.* **1998**, *114*, 435−438.
(88) Nam, S. S.; Kim, H.; Kishan, G.; Choi, M. J.; Lee, K. W. Catalytic Conversion of Carbon Dioxide into Hydrocarbons over Iron Supported on Alkali Ion-Exchanged Y-Zeolite Catalysts. *Appl. Catal., A* **1999**, *179*, 155−163.
(89) Nam, S. S.; Kishan, G.; Lee, M. W.; Choi, M. J.; Lee, K. W. Selective Synthesis of C2-C4 Olefins and C5+ Hydrocarbons over Unpromoted and Cerium-Promoted Iron Catalysts Supported on Ion Exchanged (H, K) Zeolite-Y. *J. Chem. Res., Synop.* **1999**, *5*, 344−345.
(90) Li, Z.; Wang, J.; Qu, Y.; Liu, H.; Tang, C.; Miao, S.; Feng, Z.; An, H.; Li, C. Highly Selective Conversion of Carbon Dioxide to Lower Olefins. *ACS Catal.* **2017**, *7*, 8544−8548.

DOI: 10.1021/acscatal.9b01466
ACS Catal. 2019, 9, 6320−6334